INTERNATIONAL JOURNAL FOR NUMERICAL METHODS IN FLUIDS, VOL. 19, 555–574 (1994)

NUMERICAL SIMULATION METHOD FOR VISCOELASTIC FLOWS WITH FREE SURFACES—FRINGE ELEMENT GENERATION METHOD

TORU SATO* AND STEPHEN M. RICHARDSON

Department of Chemical Engineering and Chemical Technology, Imperial College, London SW7 2BY, U.K.

SUMMARY

To simulate filling flow in injection moulding for viscoelastic fluids, a numerical method, based on a finite element method and a finite volume method, has been developed for incompressible isothermal viscoelastic flow with moving free surfaces. The advantages of this method are, first, good applicability to arbitrarily shaped mould geometries and, second, accurate treatment for boundary conditions on the free surface. Typical filling flows are simulated, namely filling flow into a 1:4 expansion cavity with and without an obstacle. Numerical results predict the position of weld lines and air-traps. The method also indicates the effects of elongational flow on molecular orientation.

KEY WORDS Finite element/finite volume method Free surface Viscoelastic flow Injection moulding

1. INTRODUCTION

To date, many numerical simulation methods have been developed and applied to fluid problems with free surfaces. The difficulties with such moving free surface problems lie in the treatment of the kinematics and boundary conditions on the free surface. Here we focus on moving free surfaces such as those in the filling process in injection moulding. In terms of numerical simulation of the filling process, several numerical codes are already available: their objectives are mainly to simulate the filling of relatively thin mould cavities. Therefore all of them make use of the Hele–Shaw approximation and ignore flow in the direction of the thickness of the cavities. Sometimes these methods are called 2·5D simulations, because the mould shape, which is intrinsically 3D, comprises 2D shells. We are, however, more interested in the details of free surface movement in relatively thick cavities than in the whole filling process of complex, if effectively zero-thickness, cavities. For a thick mould product the transverse fluid movement often determines its structural properties as well as the productivity of the moulding process.

There are several ways of treating moving free surfaces. They are well reviewed in Reference 1. Here we categorize them from a point of view considering geometrical applicability and accuracy of boundary conditions. The first category comprises methods moving the mesh system itself in a Lagrangian sense following the movement of the fluid (see e.g. Reference 2, p. 532). The concept originates in large-deformation problems in numerical structural analysis. This type of method is mainly used in a finite element formulation because it retains a desirable feature of the finite element methods: boundary conditions for the free surface are automatically

* Author to whom correspondence should be addressed. Present address: Process Engineering Development Department, Bridgestone Corporation, 3-1-1 Ogawa-Higashi, Kodaira-shi, Tokyo 187, Japan.

CCC 0271–2091/94/190555–20

Received July 1993
Revised April 1994

satisfied when the free surface is identically located on the element boundary. Another advantage is the fact that the advective term does not need to comprise a material derivative in a Lagrangian formulation. On the other hand, contact of fluid against cavity walls needs special consideration, because mesh systems do not fit the considered whole spatial domain in advance and fluids do not 'know' the position of the wall.

This method involves an essential difficulty for application to fluid dynamics: deformation of fluids is far larger than that of elastic materials and, in the course of time, the moving mesh system suffers a huge distortion. The only remedy may be re-meshing the distorted mesh system. Two re-meshing schemes were developed for flows involving the convective term by Wang and McLay.[3] The first scheme is interpolation of field variables from a distorted mesh to a reformed mesh, though interpolation always includes a truncation error. The second is to incorporate the speed of the moving mesh into the convective term. In this method the mesh movement follows some rule so that the deformed mesh is no longer distorted. Debbaut *et al.*[4] developed a method which makes use of the second kind of re-meshing to apply to the simulation of blow moulding. In their method the mesh system does not move in a Lagrangian manner but along spines radially directed to the mould walls. The mould shape of blow moulding is, however, simple compared with that of injection moulding, at least in the sense that the geometrical topology hardly changes during flow.

In the second category the mesh system is fixed in the considered spatial domain and free surfaces are treated somehow in border meshes between filled and empty meshes. Methods in this category have been favoured for application in more complex geometries such as injection moulding. The first type of this category is to solve a first-order transport equation for a volume fraction (in other words, a pseudo-concentration or a fill factor) of fluid in an element or a control volume for determining the position of the free surface. Thompson[5] developed a method of this type and applied it to filling flow in injection moulding, deformation during compression, convection of a two-layer flow and so on. In his method a low-viscosity artificial material is put in the part where a real fluid is not filled. Hence special treatment is necessary to avoid the influence of the artificial material on the flow of the real fluid when the artificial material is trapped in the real fluid or at the corner of the flow channel. A numerical solver for the first-order transport equation always requires artificial diffusion to stabilize the calculation. This sometimes makes the position of the free surface obscure, because the calculated gradient of the filling factor, which should be very steep at the free surface, is smeared out. Nassehi[6] employed the streamline upwind Petrov–Galerkin method of Brooks and Hughes[7] to avoid at least diffusion in the direction normal to the streamline.

The second type of this category is to calculate the volume fraction by using a control volume: the velocity field is used to compute the volume of fluid entering or leaving a control volume. The pioneer work was done by Tadmor *et al.*[8] for Hele–Shaw flows. Their finite difference simulation, named the FAN (flow analysis network) method, does not determine the exact position of the free surface but identifies which finite difference cells contain the free surface. Wang *et al.*[9] developed a finite element simulation method based on the idea of FAN. They employed three-node triangular elements for calculation of the flow and polygonal control volumes surrounding vertex nodes for computation of the volume fraction. The boundary condition for the free surface is approximated by setting the pressure to zero at nodes whose control volume is partially filled. Methods of this type are easy to write as computer codes and economical to run, so that many similar methods have been developed and applied to complex flow fields such as injection moulding. Osswald and Tucker[10] developed a similar technique to apply economically to compression moulding. It must be noted that the boundary condition for the free surface of this type of method is inaccurate; however, it seems that this type is

practical enough for 2·5D filling simulation using the Hele–Shaw approximation in thin mould parts.

The MAC (marker and cell) method, originally developed by Harlow and Welch,[11] has already been applied to the simulation of polymer flows with a free surface by several researchers such as Kamal *et al.*[12] and Gogos *et al.*[13] This MAC method is often used in a finite difference formulation, because finite elements do not have sufficient flexibility in shape functions. It is quite useful that the mesh system covers the whole region of a cavity where fluids may reach and that the position of the free surface is determined explicitly. The only disadvantage of this method is that boundary conditions for the free surface are normally satisfied only at discrete points, not along the whole surface, even if treated accurately in a mathematical sense.

Osswald and Tucker[14] developed a mould-filling simulation method for Hele–Shaw flows in flat uniform-thickness parts of otherwise arbitrary shape. Their method made use of a local mesh-stretching technique whereby elements including the free surface are stretched to fit their faces to the free surface at every time step. This method can be applied to complex geometries, because the mesh system is fixed in the whole domain in advance. Another advantage of this method is its accurate treatment of boundary conditions for the free surface, because mesh faces coincide with the free surface. Despite the complex procedure to deform the mesh to fit to the free surface, their simulation results for the transient position of the free surface are in good agreement with experiments.

In order also to take both the above advantages, here a new simulation method for moving free surface problems, named the *fringe element generation method*, has been developed. The original mesh system is fitted to the whole domain. New fringe elements are generated at the fringe of the free surface temporarily at each time step and so boundary conditions for the free surface are accurately satisfied, because element faces coincide with the edge of the fluid. The essential difference of the fringe element generation method from local re-meshing/stretching methods is that it *never* deforms the mesh system but instead generates new elements inside the original mesh. The fringe element generation method is incorporated into the method of Sato and Richardson,[15] which has been used successfully to simulate a number of viscoelastic benchmark problems.

2. FRINGE ELEMENT GENERATION METHOD

Fringe elements

At first, original elements are generated in the whole domain of a mould cavity. Each element has a volume fraction of fluid and each node has a flag that indicates whether it is inside the fluid or not. If all nodes have flags valued 1, the volume fraction is 1: this element is filled with fluid. If all nodes have flags valued 0, the element is empty and the volume fraction is 0. A free surface exists in elements whose volume fractions are less than 1 and greater than 0. When the free surface penetrates the original mesh system, the intersection points between the free surface and element faces become new nodes for the fringe elements. Figure 1 shows a schematic view of the fringe elements, denoted by the symbol 'x'. The bold line is the free surface and dashed lines are the original mesh system. In the fringe element generation method the free surface is approximated by a piecewise linear segment in each element and such a segment becomes a face of the fringe elements. Figure 2 shows three types of fringe elements generated in an original element: (a) a linear triangular element, (b) a bilinear quadrilateral element and (c) three linear

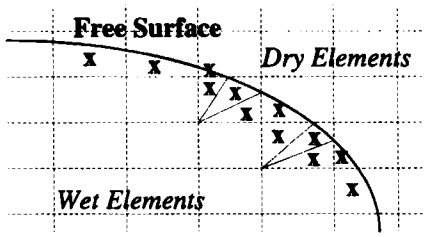

Figure 1. Fringe elements in original mesh system

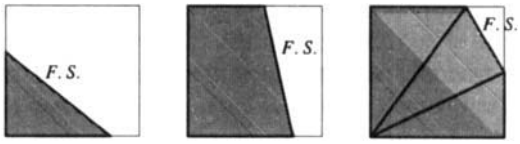

Figure 2. Three types of generation of fringe elements in an original element

triangular elements. Each box denotes an original element, bold lines denote the free surface and the area filled with fluid is shown hatched in Figure 2.

Tracing the free surface

From the nodal flag information the position of the free surface is roughly known, because the free surface always penetrates the original element through two faces that have different nodal flags, 0 and 1, at the edge of each of them. To determine the precise position of the intersection between the free surface and element faces, the volume fraction of fluid in each original element is used during tracing of the free surface. Tracing of the free surface starts at a contact point between the free surface and the wall, the position of which is known by a method described later. If one edge of the linear free surface segment is known, the other edge is simply computed by using the volume fraction. After starting with the initial position on the wall, this process is continued and the free surface is traced element-by-element until the edge of the free surface reaches a boundary of the domain of calculation. Therefore the free surface is always piecewise continuous. Moreover, the free surfaces can divide into several parts and they can never cross each other.

When the free surface has a small radius of curvature in an element, it is hard to approximate it with a linear segment. In such an element an edge of the segment calculated by the volume fraction cannot lie in a proper place. This fictitious placing of the free surface sometimes induces a geometrical oscillation of the free surface, even if the velocity field is completely oscillation-free. The best remedy may be to use a very fine mesh system where a piecewise linear approximation for the free surface is available. Unfortunately, this is quite difficult, because one cannot always predict in advance the region where the radii of curvature of the free surface are small during filling. Since this oscillation is a totally geometrical artefact, appropriate filtering or smoothing retains physical reality and never spoils the accuracy of resolution of the position of the free surface. When a zigzag mode across three elements is found, more realistic edges of the free surface segments are generated on the original mesh system by filtering. Temporarily, the volume

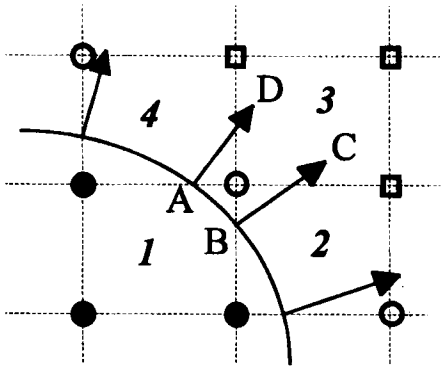

Figure 3. Advance of free surface

fraction in such an original element is not exactly consistent with the area of fringe element(s) in it; however, the correct volume fraction is always stored in computer memory and used correctly at the next time step to preserve the mass balance.

Occasionally, fringe elements which are too small are generated depending on the position of intersection points between the free surface and the original mesh system, which possibly deteriorates the speed of computation because of a CFL (Courant–Friedrichs–Lewy) stability condition.[16] In order to maintain high computational performance, the fringe element generation method provides a remedy for this unfavourable feature. In the case where a fringe node is located very close to a node of the original mesh—say the length of the element face of a fringe element is less than 5% of that of original elements—such a fringe node is merged with the original one and the fringe elements are squeezed so as to disappear. The volume fraction of such an element is, however, also stored in computer memory, so that the fringe element generation method never compromises the mass balance.

Kinematics

Forward Euler differencing with respect to time gives the kinematics of the transiently moving free surface in the fringe element generation method as

$$\mathbf{r}^{n+1} = \mathbf{r}^n + \Delta t \mathbf{v}^n, \tag{1}$$

where $\mathbf{r}^n$ is the position of the free surface at time step n and $\mathbf{v}^n$ is the velocity vector of the moving free surface calculated at position $\mathbf{r}^n$. To trace the free surface at each time step, it is necessary to calculate the increase or decrease in the volume fraction in each element and to determine the wet/dry flag on each node. In Figure 3 dashed lines denote the original mesh system, the solid line is the current position of the free surface and the dotted line is that after moving a time increment Δt. Two nodes A and B of the fringe elements are moved to C and D respectively by equation (1) using velocities calculated on A and B at time step n. In quadrilateral ABCD each area that becomes part of the original elements 1, 2, 3 and 4 is respectively added to the volume fraction of the corresponding original element. In Figure 3 wet nodes (inside the fluid) are shown by closed circles and dry ones (outside the fluid) are shown by open squares. If quadrilateral ABCD includes nodes that used to be dry, they are changed to be wet, as shown by open circles.

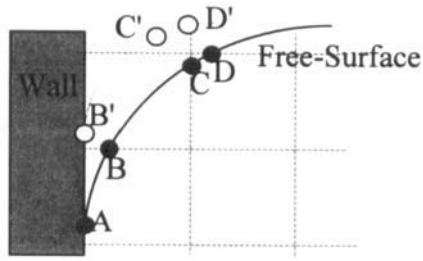

Figure 4. Contact between free surface and wall

Contact point between free surface and wall

On the wall a no-slip condition is applied and therefore the free surface rolls onto the wall satisfying this condition. Figure 4 is a schematic explanation of this process in the present method. The hatched part on the left-hand side is the wall and dashed lines denote the original mesh. The current position of the free surface is shown by a solid line and that of the next time step by a dotted line. Node A is located on the contact point between the free surface and the wall, which does not move because of the no-slip condition. If node B, the node next to A, attaches to or tries to penetrate the wall when it moves with its prescribed velocity, it sticks to that position on the wall and becomes the contact node at the next time step, which is shown by node B'. In this way the free surface advances smoothly along the wall satisfying the no-slip condition.

Extrapolation of velocity and extra stress

At the beginning of each time step of computation, new wet nodes do not yet have velocities. Here extrapolation is used for obtaining velocities at such nodes. Before the generation of new fringe elements, the average of the velocities on A and B represents the velocity of quadrilateral ABCD in Figure 3. This velocity value is integrated into original element 3 and then a volume average determines a new elemental value of velocity in element 3. After the generation of new fringe elements, since the velocity is defined on each node and not in each element, volume-averaged elemental values of the velocity are distributed into new fringe nodes by a Galerkin method, which means zeroth-order extrapolation at the edge of the computational domain. Although this is a lowest-order extrapolation, the velocity so calculated is not used directly for moving the free surface: it is modified by the result of the pressure calculation before being used for that purpose. However, attention should be paid to whether the simulation results are sensitive to mesh refinement. Linear extrapolation is also provided as an option in the present method. In the viscoelastic case the elastic stress, which advects in accordance with a constitutive equation, in each new fringe element is also obtained similarly: it is transported from the current fringe elements into the original elements, where the stress is volume averaged, and then distributed into new fringe elements.

3. FINITE ELEMENT/FINITE VOLUME FORMULATIONS FOR VISCOELASTIC FLOW

The discretization formulations of the present method are the same as those of Sato and Richardson.[15] The inelastic part of their formulations is similar to the method of Tanahashi *et*

al.,[17] which was successfully applied to high-Reynolds-number problems for Newtonian fluid flow. For viscoelastic fluid flow Sato and Richardson[15] incorporated an FCT (flux-corrected transport) algorithm to achieve TVD (total variation diminishing) in a finite volume solver for the viscoelastic constitutive equation.

The Galerkin method gives the discrete momentum equation

$$M^{\alpha\beta}v_i^{\beta n+1} = M^{\alpha\beta}v_i^{\beta} + \Delta t(-E^{\alpha\beta}v_i^{\beta} - B_j^{\alpha}\sigma_{ij} + S_i^{\alpha}), \tag{2}$$

where

$$\sigma_{ij} = -p^{n+1}\delta_{ij} + T_{ij}, \tag{3}$$

and

$$M^{\alpha\beta} = \int_V \rho\Phi^{\alpha}\Phi^{\beta}\,\mathrm{d}V, \qquad E^{\alpha\beta} = \int_V \rho v_j \frac{\partial\Phi^{\beta}}{\partial x_j}\Phi^{\alpha}\,\mathrm{d}V, \qquad B_j^{\alpha} = \int_V \frac{\partial\Phi^{\alpha}}{\partial x_j}\,\mathrm{d}V, \qquad S_i^{\alpha} = \oint_\Gamma \Phi^{\alpha}\sigma_{ij}n_j\,\mathrm{d}\Gamma. \tag{4}$$

Here Φ is a bilinear weight function, v_i is the velocity vector, σ_{ij} is the total stress tensor, p is the pressure, T_{ij} is the deviatoric stress tensor, δ_{ij} is the unit tensor, Δt is the time increment of first-order Euler time differencing, ρ is the constant density, V is the area of an element, Γ is the boundary of an element and n_j is a unit-vector component normal to the element boundary. Since σ_{ij} is approximated piecewise-constantly in each element, it is integrated out in equation (2). The fourth equation of (4) gives the boundary conditions. As often done in the time-dependent FEM, the mass matrix $M^{\alpha\beta}$ is lumped for the purpose of speed of computation.

Integration of a Poisson equation for pressure in each element gives

$$\oint_\Gamma \left(\frac{\rho}{\Delta t}v_i + \frac{\partial}{\partial x_j}(-p\delta_{ij} + T_{ij} - \rho v_i v_j)\right)\mathrm{d}\Gamma = 0. \tag{5}$$

This is a finite volume formulation of the Poisson equation. A converged solution p from an iterative solver of equation (5) is used as a right-hand side in equation (2) and a resulting solution v_i^{n+1} automatically satisfies a solenoidal condition at time step $n+1$. The second term on the left-hand side in equation (5) requires the first derivatives of elemental values on element faces Γ. To calculate the gradient of an elemental value W, subelements are introduced following Ikegawa,[18] where W is concentrated on the centroid of the element. In Figure 5 we focus on element face 12 and subelement C1S2, which is divided into two triangles C1S and CS2. The gradient of W in C1S is given by

$$\begin{aligned}\left[\frac{\partial W}{\partial x}\right]_{\mathrm{C1S}} &= \frac{1}{2S_{\mathrm{C1S}}}[(y_{\mathrm{C}} - y_1)W_{\mathrm{S}} + (y_1 - y_{\mathrm{S}})W_{\mathrm{C}} + (y_{\mathrm{S}} - y_{\mathrm{C}})w^1],\\ \left[\frac{\partial W}{\partial y}\right]_{\mathrm{C1S}} &= \frac{1}{2S_{\mathrm{C1S}}}[(x_1 - x_{\mathrm{C}})W_{\mathrm{S}} + (x_{\mathrm{S}} - x_1)W_{\mathrm{C}} + (x_{\mathrm{C}} - x_{\mathrm{S}})w^1].\end{aligned} \tag{6}$$

The gradient of W in CS2 is obtained similarly. A weighted average of gradients in C1S and CS2 gives the gradient of W in subelement C1S2. To obtain nodal values w^{β} from the elemental value W, bilinear weight functions are applied:

$$\int_V W\,\mathrm{d}V = \int_V \Phi^{\alpha}w^{\alpha}\,\mathrm{d}V. \tag{7}$$

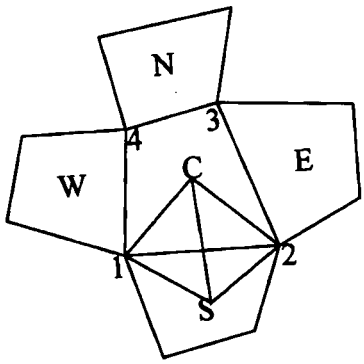

Figure 5. Elements C, E, N, W and S and subelements C1S and CS2

As a viscoelastic model an Oldroyd-B model is chosen:

$$T_{ij} = 2\eta_s D_{ij} + \tau_{ij}, \qquad D_{ij} = \frac{1}{2}\left(\frac{\partial v_i}{\partial x_j} + \frac{\partial v_j}{\partial x_i}\right), \tag{8}$$

where η_s is the Newtonian solvent viscosity and τ_{ij} is the extra stress tensor. The Oldroyd-B model is not appropriate for the description of real material flow because it has an infinite elongational viscosity at a finite extension rate and no shear-thinning property. However, this model has been a benchmark viscoelastic model for checking the robustness of numerical methods for the past decade. For the Oldroyd-B model the extra stress is obtained by solving a constitutive equation for the upper-convected Maxwell fluid. In other words, the upper-convected Maxwell fluid is a special case ($\eta_s = 0$) of the Oldroyd-B fluid. Applying the Gauss–Green theorem to the constitutive equation gives

$$\tau_{ij}^{n+1} = \left(1 - \frac{\Lambda}{\lambda}\right)\tau_{ij} - \frac{\Lambda}{V}\oint_\Gamma \tau_{ij}^{n+\theta} v_k n_k \, d\Gamma + \frac{\Lambda}{V}\left[\left(\tau_{ik}^{n+\theta} + \frac{\eta_p}{\lambda}\delta_{ik}\right)\oint_\Gamma v_j n_k \, d\Gamma + \left(\tau_{jk}^{n+\theta} + \frac{\eta_p}{\lambda}\delta_{jk}\right)\oint_\Gamma v_i n_k \, d\Gamma\right], \tag{9}$$

where

$$\Lambda = \frac{\Delta t}{\lambda + \theta \Delta t}\lambda. \tag{10}$$

Here λ is the relaxation time and η_p is the polymer viscosity. The stress is integrated out because it is approximated piecewise-constantly in each element. When $\theta = 1$, equation (9) has first-order accuracy with respect to time; when $\theta = \frac{1}{2}$, it has second-order accuracy. The second term on the right-hand side of equation (9) is the advective term, which includes the stress values on element faces. We apply an FCT concept, originally developed by Boris and Book,[19] to our method to achieve TVD. A TVD scheme guarantees no spurious oscillations, which otherwise appear near the steep gradients of field variables, e.g. near a sharp corner. In the present method donor-cell-type upwinding is a lower-order TVD scheme and second-order central differencing is a higher-order one. A flux limiter due to Zalesak[20] for multiple dimensions is adopted in the present method for antidiffusion. The FCT algorithm gives sufficient artificial diffusion to smooth unphysical extrema *locally* only where it is necessary.

4. BOUNDARY AND INITIAL CONDITIONS

Boundary conditions that specify velocity components are applied to the wall where we assume no slip and to the inlet where the flow rate is specified. At the centre plane the flow is assumed to be symmetrical. The present time-dependent finite volume method needs boundary values of the stress at all element faces including the inflow either in a Dirichlet or a Neumann sense. A homogeneous Neumann condition (zero gradient) is adopted at the inflow boundary provided that it is far from flow disturbances.

One of the advantages of using a finite element method is its simple treatment of boundary conditions on the free surface. On the free surface we can assume

$$\sigma_{ij} n_j = o_i. \tag{11}$$

Here surface tension is ignored. By equation (11), the fourth equation of (4) explicitly vanishes. The fringe element generation method retains this advantage because it coincides with the boundaries of the fringe elements.

In the present method a Poisson equation for pressure is solved so that the solenoidal condition (divergence-free velocity field) is satisfied. Equation (11) gives a sufficient condition for determining the pressure on the free surface. Here only its component normal to the free surface is considered and a Dirichlet condition is given on the free surface to the finite volume formulation of the Poisson equation for pressure, (5):

$$p = T_{ij} n_i n_j = (2\eta_s D_{ij} + \tau_{ij}) n_i n_j. \tag{12}$$

At an inflow boundary, a wall boundary or a symmetric boundary a Newmann condition on pressure is set and thus the free surface is the only boundary to give reference values for the pressure. To obtain pressure values at nodes on the free surface, extra stress components are distributed from the elements on to the nodes by equation (7). By using these nodal values of the stress, equation (12) gives a nodal value of the pressure. In Figure 6 a normal vector at node B is regarded as an average of those of AB and BD.

Subelements for the present pressure solver along the free surface are shown in Figure 6. Dashed lines denote the original mesh and bold solid lines denote faces of the fringe and original elements. Fine solid lines are faces of the subelements, the nodes of which are the original nodes including the fringe nodes and centre points of the elements shown by open circles. At the free

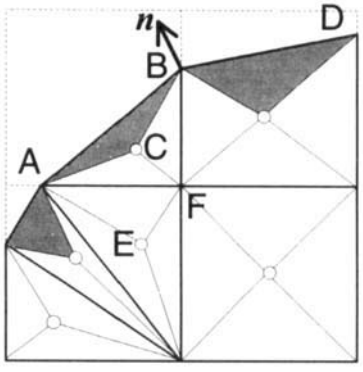

Figure 6. Subelements along free surface

surface the subelements are triangular like ACB. The constant gradients inside subelement ACB, which are assumed to be the first derivatives on free surface segment AB, are calculated by

$$\left[\frac{\partial W}{\partial x}\right]_{AB} = \frac{1}{2S}[(y_B - y_A)W_C + (y_A - y_C)w_B + (y_C - y_B)w_A],$$
$$\left[\frac{\partial W}{\partial y}\right]_{AB} = \frac{1}{2S}[(x_A - x_B)W_C + (x_C - x_A)w_B + (x_B - x_C)w_A], \tag{13}$$

where S is the area of triangle ACB.

Initial conditions should be compatible with the inflow boundary condition to make the simulation physically meaningful: here the fully developed flow condition is used as the initial condition for both velocity and stress.

5. CASE STUDIES FOR FILLING FLOW IN INJECTION MOULDING

Filling flow into 1 : 4 expansion

First, the present method is applied to filling flow into a 1 : 4 expansion cavity. Here annular mould cavities like those shown in Figure 7 are considered and only the section enclosed by dashed lines is the subject of simulation. In Figure 7 a quarter part is cut to show the inside and the cavity channel is denoted by hatching. Since the radius of the annular cavity is quite large compared with its thickness, flow into such a cavity can be regarded as two-dimensional without any azimuthal (angular) variation. Engineering interest lies in the motion of the free surface to predict the possible position of air-traps. Vent-holes should be provided on the mould surface in accordance with this prediction. Another interest lies in the molecular orientation distribution.

Figure 8 shows a schematic domain of computation for filling flow into a 1 : 4 expansion mould cavity including the initial position of the melt front. Based on the assumption of

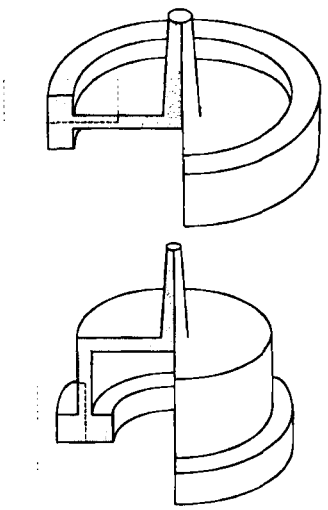

Figure 7. Annular mould cavities

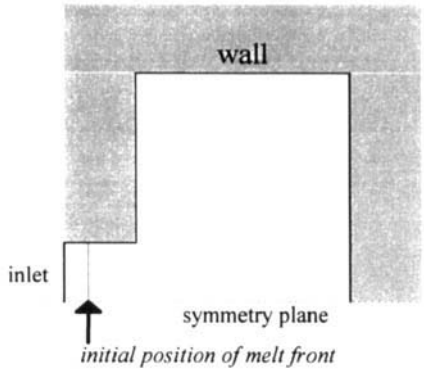

Figure 8. Schematic of computational domain of 1:4 expansion cavity

symmetry, the computational domain is half of the cavity. The size of the half-cavity is $3h \times 4h$ (length × height), where h is the half-thickness of the sprue and the gate. The computational domain also has a sprue, the length of which is h. Since the shape of the fully developed free surface is unknown, a straight line perpendicular to the gate wall is used. This involves incompatibility with the initial condition for the stress and causes failure of the present simulation especially for high We. This is described at the end of this subsection.

Non-dimensional numbers which determine Oldroyd-B fluid flows are the Reynolds number Re, the Weissenberg number We and the ratio a between the solvent viscosity and the total viscosity:

$$Re = \frac{\rho U h}{\eta_s + \eta_p}, \qquad We = \lambda \frac{U}{h}, \qquad a = \frac{\eta_s}{\eta_s + \eta_p}. \tag{14}$$

Figures 9(a) and 9(b) show advancing melt fronts of Oldroyd-B fluids during filling for $We = 1$ and 2 respectively at $Re = 10$ and $a = 0{\cdot}5$. The non-dimensional numbers are based on the mean velocity U inside the sprue and the half-thickness h of the sprue part. Solid lines give the shape of the free surfaces plotted at every 10% of the total volume of the mould cavity and dotted lines show the original mesh system initially generated inside the whole mould cavity. The original elements are of size $0{\cdot}2h \times 0{\cdot}2h$. In Figure 9(a) the melt front advances straight to the front wall and then changes course towards the upper wall after hitting the front wall. As a result the region very close to the side of the gate is filled at the last stage of filling for $Re = 10$. On the other hand, in Figure 9(b) the main flow passes the centre of the cavity after hitting the front wall. In this case the last part filled with fluid is the top left corner. Viscoelastic fluids have a normal stress difference due to shear along the wall when they flow through a narrow sprue. The normal stress difference results in so-called extrudate swell, the phenomenon whereby the radius of extrudates is larger than that of the die immediately after the flow exits the gate. This effect, which is larger in a more elastic case, is seen in the comparison between Figures 9(a) and 9(b).

Figure 10(a) shows contour plots of the principal stress difference for an Oldroyd-B fluid with $Re = 10$, $We = 2$ and $a = 0{\cdot}5$ at the moment of 90% filling of the whole cavity volume. The principal stress difference $\Delta\tau$ is defined by

$$\Delta\tau = \sqrt{[(\tau_{xx} - \tau_{yy})^2 + 4\tau_{xy}^2]}, \tag{15}$$

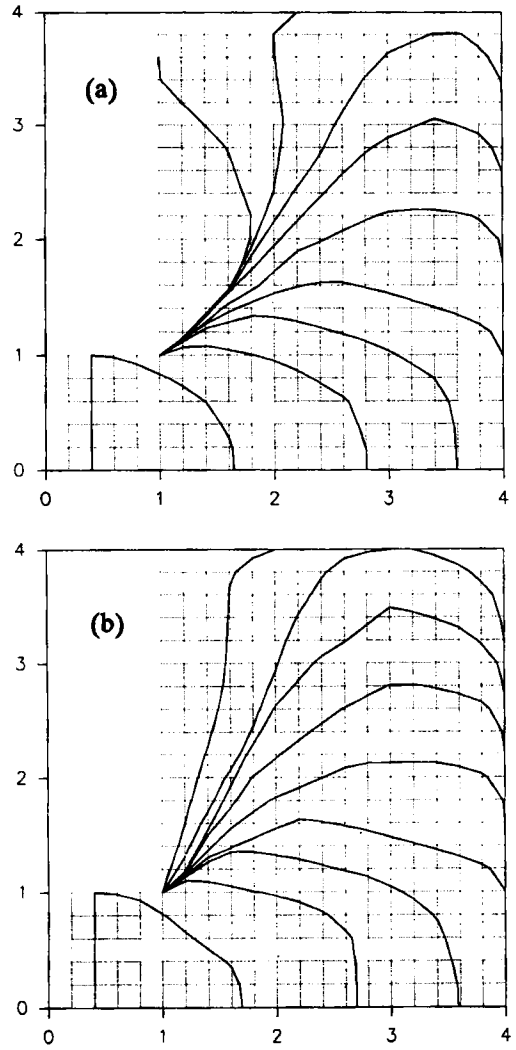

Figure 9. Advancing melt front plotted at every 10% of cavity volume during filling for Oldroyd-B fluids with $Re = 10$, $a = 0{\cdot}5$ and (a) $We = 1$, (b) $We = 2$

where τ_{xx} and τ_{yy} are the normal stress components and τ_{xy} is the shear stress component. Since amorphous polymers have entropic elasticity, the principal stress difference is a quantitative measure of molecular orientation. Figure 10(a) therefore indicates the degree of molecular orientation at the moment of 90% filling. Contour lines of the principal stress difference give two high parts along the gate wall and near the front wall. The former may be due to high shear at the wall of a narrow channel. Since the highest value is not given on the front wall for the latter case, it is not due to shear at the wall. The high values of $\Delta\tau$ near the front wall may be due to elongation on the symmetric centreline, where the flow bifurcates to two symmetric parts of the cavity. Figure 10(b) is a schematic view of the molecular orientation, in which the length of each segment corresponds to the value of the principal stress difference and the direction

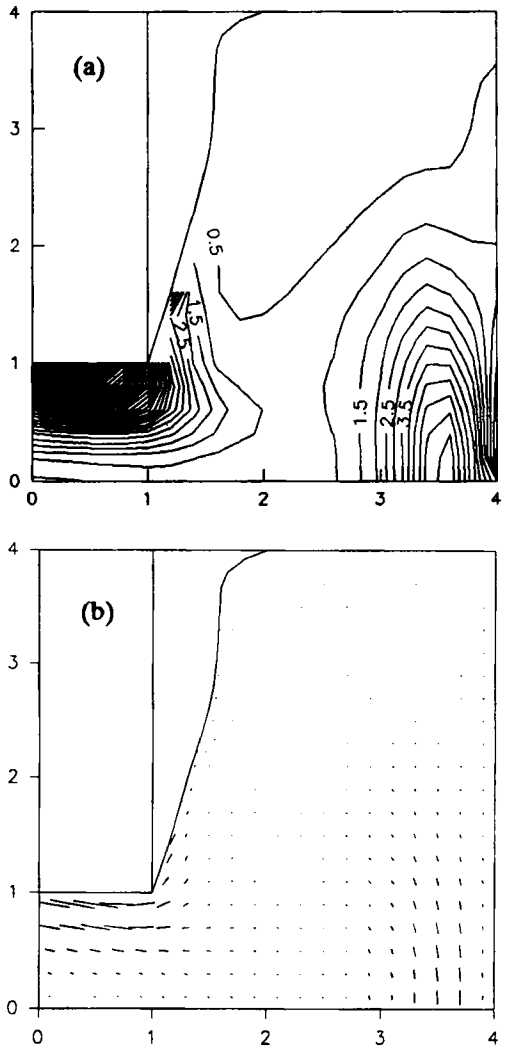

Figure 10. (a) Contour plots of principal stress difference and (b) schematic view of molecular orientation at instance of 90% filling for Oldroyd-B fluid with $Re = 1$, $We = 2$ and $a = 0{\cdot}5$

corresponds to that of the maximum principal stress, which is given by the angle ψ measured from the x-axis:

$$\tan(2\psi) = \frac{2\tau_{xy}}{\tau_{xx} - \tau_{yy}}. \tag{16}$$

Figures 11(a) and 11(b) show an advancing melt front and a contour plot of the principal stress difference respectively for an Oldroyd-B fluid with $Re = 10$, $We = 2$ and $a = 0{\cdot}5$, which is the same flow as those of Figures 9(b) and 10(a). Here a finer mesh ($0{\cdot}143h \times 0{\cdot}143h$) is used. The shape of the advancing melt front during filling in Figure 11(a) is almost the same as that of Figure 9(b), while the finer mesh can represent smaller radii of curvature of the free surface. In comparison between Figures 10(a) and 11(b), the coarse mesh seems to have numerical

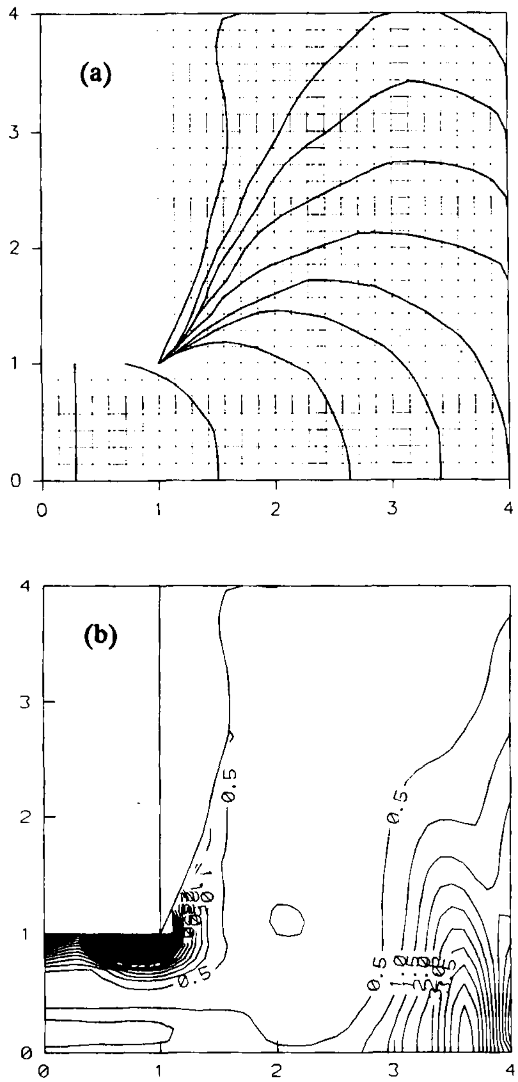

Figure 11. (a) Advancing melt front plotted at every 10% of cavity volume during filling and (b) contour plots of principal stress difference at instance of 90% filling for Oldroyd-B fluid with $Re = 10$, $We = 2$ and $a = 0{\cdot}5$ in finer mesh

diffusion in the stress field because of its poorer spatial resolution: Figure 11(b) shows steeper gradients of the stress. However, the highest values in each contour island and the positions of these values are essentially the same. These facts may give validity to the present simulation in the sense that there is no mesh dependence.

The upper limit on *We* is found to be a little above 2 for the Oldroyd-B fluid in this flow. Although the computation does not diverge, results show unphysically large values of stress and pressure along the gate wall near the inflow. The problem may be partially due to incompatibility between the initial condition for the stress and the initial position of the melt front. On the free surface, pressure is given in a Dirichlet sense by equation (12). If the initial position of the free

surface is a line parallel to the thickness direction, a normal unit vector **n** to the free surface has components

$$n_x = 1, \qquad n_y = 0. \tag{17}$$

Therefore the pressure on the free surface is given by

$$p = T_{xx} = \eta_s \frac{\partial v_x}{\partial x} + \tau_{xx}. \tag{18}$$

The initial condition is set as a fully developed flow; hence v_x is constant in the x-direction and τ_{xx} has a parabolic profile in the y-direction. Consequently we get

$$p = \tau_{xx} = \frac{18\lambda\eta_p U^2}{h^4} y^2. \tag{19}$$

However, the fully developed condition based on a Poiseuille flow has a constant pressure in the y-direction with a constant pressure gradient in the x-direction. This contradiction is due to the wrong initial position of the free surface. In a real flow, if the flow is cut perpendicular to the flow direction, the free surface may immediately change its shape because of the residual stress, which is exactly the extra elastic stress at the moment when it gets cut. This incompatibility between the initial stress and the initial position of the free surface already exists even for small-*We* cases. However, it seems that there is little significant effect when λ in equation (19) is small.

A better initial condition should be the use of a plausible initial position of the free surface such as the result of fountain flow simulation. Otherwise, it may be sensible to provide a long sprue, in which a fully developed fountain flow is expected, and to set zero stress as the initial condition and zero-gradient stress as the inflow boundary condition. Mesh refinement may also be effective in increasing *We*; however, such an effect is limited to the slight increase as studied in Figure 11.

Filling flow into 1 : 4 expansion with an obstacle

Second, the method is applied to flow around an elliptic obstacle in the 1 : 4 expansion cavity. The schematic computational domain is shown in Figure 12. Here engineering interest lies in the position of a so-called weld line in addition to the distribution of molecular orientation or

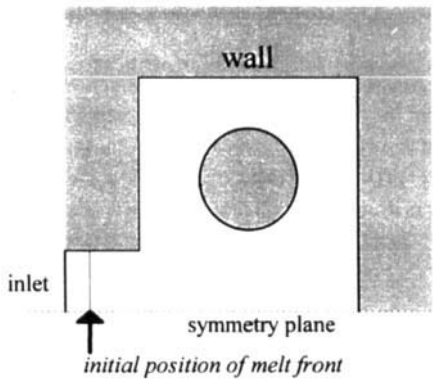

Figure 12. Schematic of computational domain of 1 : 4 expansion cavity with obstacle

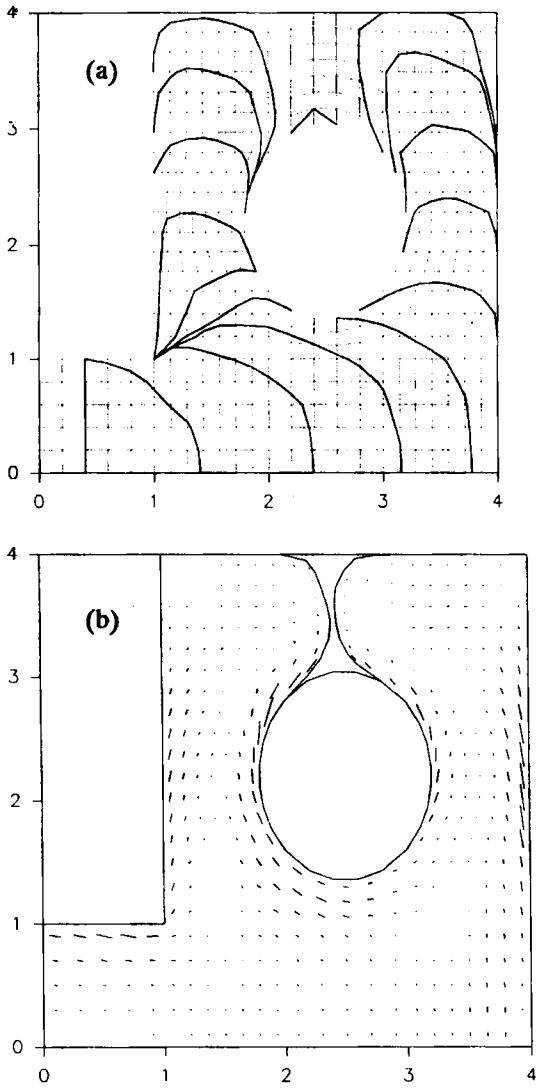

Figure 13. (a) Advancing melt front at every 10% of cavity volume and (b) schematic view of molecular orientation at instant of 95% filling for Oldroyd-B fluid with $Re = 10$, $We = 1$ and $a = 0{\cdot}5$

the position of air-traps. When two advancing melt fronts meet together behind an obstacle inside a mould cavity, the interface between them is called a weld line, which is sometimes clearly observed on the surface of moulded products even if the two free surfaces are formed of the same material. The problem is not only the bad appearance of the products but also the fracture weakness along the weld line. Therefore it is important to control the position of the weld line by design of a mould system, including the position of gates. In general, the weld line is a line in the flow-width plane observed on the surface of thin moulded products, though Figure 12 shows a cut section in the flow-thickness direction of an annular/long-straight mould cavity. However, it is also a weld line in the sense that fracture weakness is anticipated there.

Figure 13(a) shows an advancing melt front at every 10% of cavity volume and at the instant

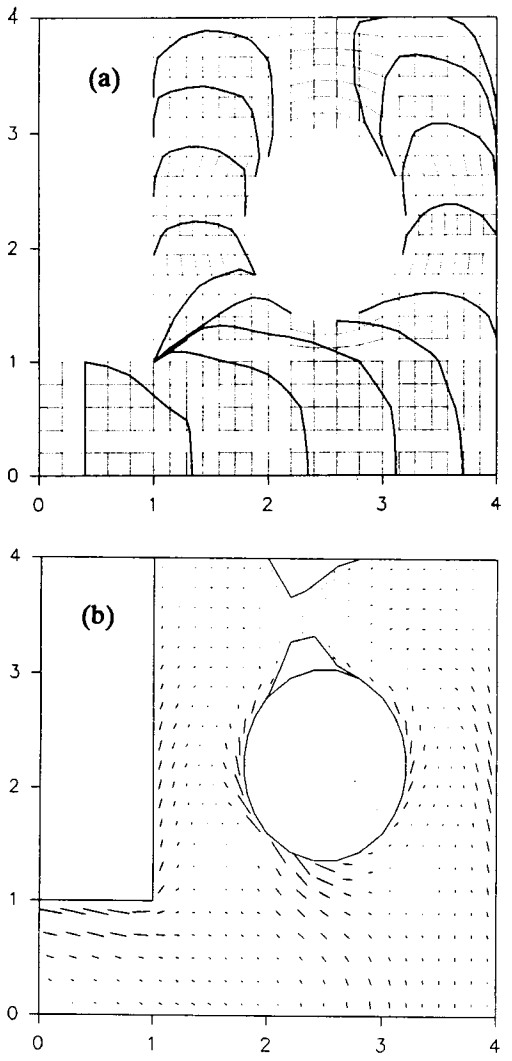

Figure 14. (a) Advancing melt front at every 10% of cavity volume and (b) schematic view of molecular orientation at instant of 95% filling for Oldroyd-B fluid with $Re = 1$, $We = 1$ and $a = 0{\cdot}5$

of 98% filling and Figure 13(b) a schematic view of the molecular orientation based on the principal stress difference at the moment of 95% filling for an Oldroyd-B fluid with $Re = 10$, $We = 1$ and $a = 0{\cdot}5$. In Figure 13(a) the melt front entering the cavity is divided into two parts when it reaches the obstacle, which meet together after passing the obstacle at the top of the cavity. In Figure 13(b) high orientation is observed along walls including those of the obstacle. Because of the existence of the obstacle, the effective flow channel in the cavity becomes narrow and hence shear along the wall seems to dominate the orientation of molecules.

Figures 14(a) and 14(b) show an advancing melt front and the molecular orientation respectively for an Oldroyd-B fluid with $Re = 10$, $We = 2$ and $a = 0{\cdot}5$. The position of the advancing melt front is almost the same in Figure 13(a) as in Figure 14(a); consequently the position of the weld line is almost the same. In Figure 14(b) the molecular orientation trend

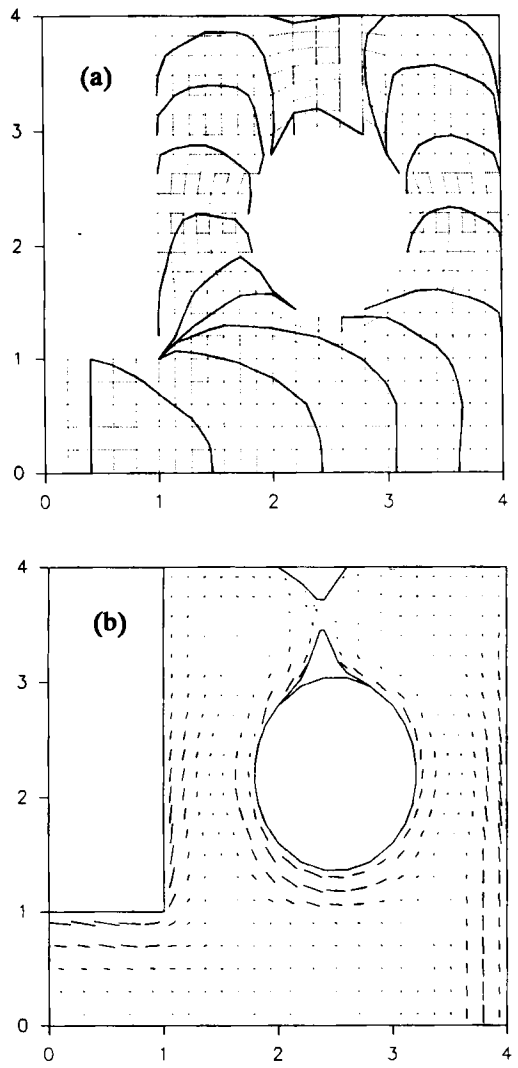

Figure 15. (a) Advancing melt front at every 10% of cavity volume and (b) schematic view of molecular orientation at instant of 95% filling for upper-convected Maxwell fluid with $Re = 10$ and $We = 1$

observed in Figure 13(b) becomes much clearer. At the same time, on the symmetric centre near the front (right) wall, high orientation resulting from elongation in the bifurcating (symmetric) flow is observed.

Figures 15(a) and 15(b) show an advancing melt front and the molecular orientation respectively for an upper-convected Maxwell fluid with $Re = 10$ and $We = 1$. The melt front moves similarly to the Oldroyd-B cases. A slight change is seen at the position of the weld line in Figure 15(a): this time it is located a little closer to the gate. Since the fluid does not have a retardation time, stresses respond to flow deformation instantaneously. Unlike the Oldroyd-B fluids, high orientation resulting from elongation in a radial flow (perpendicular to the flow) is seen just under the obstacle in Figure 15(b).

6. CONCLUSIONS

A new method for moving free surfaces has been developed and incorporated into a flow simulation method for viscoelastic fluids. This method, which is called the fringe element generation method, has two main advantages. The first is good applicability to arbitrarily shaped mould cavities: original elements are provided in the whole cavity from the beginning and hence there is no need to make the flow perceive the position of complex mould walls. The second is accurate treatment of boundary conditions for the free surface in the finite element formulation for the momentum equation: fringe elements are generated along the free surface temporarily at every time step and the free surface always coincides with their faces.

The present numerical simulation method has been carried out for viscoelastic flow problems including a moving free surface, namely filling flow into 1:4 expansion both with and without an obstacle. The solutions exhibit no mesh dependence. The method predicts the position of weld lines, the position of air-traps, the values of residual stress and the degree and direction of molecular orientation. Moreover, the simulations suggest that the effects of elongational flow are significant on molecular orientation.

Unfortunately, no experiments using real materials have been done to compare with the present simulations. It is also very difficult to find experimental results similar to the present simulation conditions in the literature, partly because injection moulding with thin parts has been the centre of industrial interest so far.

ACKNOWLEDGEMENT

One of the authors (T.S.) has been financially supported by the Bridgestone Corporation.

REFERENCES

1. H. P. Wang and H. S. Lee, 'Free and moving boundary problems', in C. L. Tucker III (ed.), *Fundamentals of Computer Modeling for Polymer Processing*, Hanser, Munich, 1989.
2. O. C. Zienkiewicz and R. Taylor, *The Finite Element Method*, Vol. 2, 4th edn, McGraw-Hill, London, 1991.
3. H. P. Wang and R. T. McLay, 'Remeshing schemes for convective elements with applications to hot forming processes', *Proc. 5th Int. Symp. on Finite Elements and Flow Problems*, 1984, pp. 521–526.
4. B. Debbaut, B. Hocq and J. M. Marchal, 'Numerical simulation of the blow molding process', *SPE Antec Papers*, **32**, 1870–1872 (1993).
5. E. Thompson, 'Use of pseudo-concentration to follow creeping viscous flows during transient analysis', *Int. j. numer. methods fluids*, **6**, 749–761 (1986).
6. V. Nassehi, 'The free surface tracking in viscoelastic flow', *Int. j. numer. methods eng.*, in press.
7. A. N. Brooks and T. J. R. Hughes, 'Streamline-upwind Petrov/Galerkin formulations for convection dominated flows with particular emphasis on the incompressible Navier–Stokes equations', *Comput. Methods Appl. Mech. Eng.*, **32**, 199–259 (1982).
8. Z. Tadmor, E. Broyer and C. Gutfinger, 'Flow analysis network (FAN)—a method for solving flow problems in polymer processing', *Polym. Eng. Sci.*, **14**, 660–665 (1974).
9. V. H. Wang, C. A. Hieber and K. K. Wang, 'Mold filling simulation in injection molding of three-dimension thin parts', *SPE Antec Tech. Papers*, **32**, 97–102 (1986).
10. T. A. Osswald and C. L. Tucker III, 'Compression mold filling simulation for non-planar parts', *Int. Polym. Process.*, **5**, 79–87 (1990).
11. F. H. Harlow and J. E. Welch, 'Numerical calculation of time-dependent viscous incompressible flow of fluid with free surface', *Phys. Fluids*, **8**, 2182–2189 (1965).
12. M. R. Kamal, E. Chu, P. G. Lafleur and M. E. Ryan, 'Computer simulation of injection mold filling for viscoelastic melts with fountain flow', *Polym. Eng. Sci.*, **26**, 190–196 (1986).
13. C. G. Gogos, C.-F. Huang and L. R. Schmidt, 'The process of cavity filling including the fountain flow in injection molding', *Polym. Eng. Sci.*, **26**, 1457–1466 (1986).
14. T. A. Osswald and C. L. Tucker III, 'An automated simulation of compression mold filling for complex parts', *SPE Antec Tech. Papers*, **31**, 169–172 (1985).
15. T. Sato and S. M. Richardson, 'Explicit numerical simulation of time-dependent viscoelastic flow problems by a finite element/finite volume method', *J. Non-Newtonian Fluid Mech.*, **51**, 249–275 (1994).

16. T. Sato, 'Numerical study of viscoelastic flow problems in injection moulding', *Ph.D. Thesis*, University of London, 1993.
17. T. Tanahashi, H. Okanaga and T. Saito, 'GSMAC finite element method for unsteady incompressible Navier–Stokes equations at high Reynolds numbers', *Int. j. numer. methods fluids*, **11**, 479–499 (1990).
18. M. Ikegawa, 'A new finite element technique for the analysis of steady viscous flow problems', *Int. j. numer. methods eng.*, **14**, 103–113 (1979).
19. J. P. Boris and D. L. Book, 'Flux-corrected transport. I. SHASTA, a fluid transport algorithm that works', *J. Comput. Phys.*, **11**, 38–69 (1973).
20. S. T. Zalesak, 'Fully multidimensional flux-corrected transport algorithm for fluids', *J. Comput. Phys.*, **31**, 335–362 (1979).